Journal of Materials Chemistry B

Accepted Manuscript

ROYAL SOCIETY OF CHEMISTRY

www.rsc.org/materialsB

A novel 3D porous network-structured tissue engineering scaffold built of mesoporous TiO_2 nanotubes has been synthesized via the bacterial cellulose-templated sol-gel route followed by calcination.

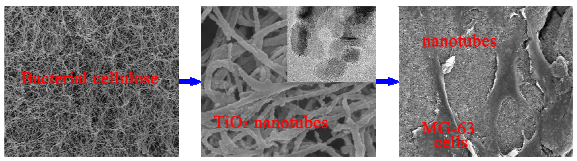

Constructing a novel three-dimensional scaffold with mesoporous TiO_2 nanotubes for potential bone tissue engineering

Yizao Wan [a,b], Zhiwei Yang [b], Peng Chang [b], Guangyao Xiong *[a], Ping Liu [b], Honglin Luo *[b]

[a] *School of Mechanical and Electrical Engineering, East China Jiaotong University, Nanchang 330013, China*

[b] *School of Materials Science and Engineering, Tianjin University, Tianjin Key Laboratory of Composite and Functional Materials, Tianjin 300072, China*

Abstract

Three-dimensional (3D) nanofibrous scaffolds for tissue engineering have been widely studied while 3D scaffolds made from nanotubes are rarely reported. Herein, we report a novel 3D porous network-structured scaffold built of mesoporous TiO_2 nanotubes. The TiO_2 nanotubes were synthesized using the template-assisted sol-gel method followed by calcination. Bacterial cellulose (BC) with 3D network structure was used as the template. TEM observation confirms the formation of tubular TiO_2 nanotubes. The as-synthesized TiO_2 nanotubes exhibit an average outer diameter of less than 100 nm and mesoporous walls consisting of aggregated TiO_2 nanoparticles with a size of around 7 nm. SEM and TEM observations reveal that the TiO_2 nanotube scaffold possesses 3D porous network structure and the surfaces of TiO_2 nanotubes are rugged with nanotopography. Additionally, the scaffold built of mesoporous nanotubes with a mesopore size of 3.3 nm exhibits extremely large surface area of

1629 m^2 g^{-1}. The capacity of the scaffold to support cell proliferation and osteogenic differentiation was evaluated using CCK-8 assay, alkaline phosphatase (ALP), and calcium content assay. The scaffold shows enhanced cell growth and proliferation and improved ALP activity and mineralization compared to the TCPS (tissue culture plate) control. Furthermore, the ALP activity of the scaffold is as high as a hydroxyapatite-coated nanofibrous scaffold. The enhanced proliferation and osteogenic differentiation of the TiO_2 nanotube scaffold is ascribed to the outer surface roughness of TiO_2 nanotubes, 3D porous network structure, mesopores, and large surface area.

1 Introduction

Nanostructured titanium dioxide (TiO_2) has been widely used in various applications such as photo-splitting of water,[1] photocatalysis,[2, 3] biosensors,[4] solar cells,[5, 6] rechargeable lithium batteries,[7] and biomaterials.[8, 9] Therefore, much effort has been devoted to the synthesis of nanostructured TiO_2 such as nanoparticles, nanofibers, nanowires, nanorods, and nanotubes due to their high surface-to-volume ratio and the potential for unique new material properties and applications in a wide range of areas[10, 11]. Among these TiO_2 nanostructures, tubular TiO_2 has attracted much attention due to their improved properties in many applications compared to nanofibers, colloids, films, and other forms of TiO_2[7, 12] and the ability to mimic the dimensions of constituent components of natural bone.[13] In the field of biomedical engineering, TiO_2 nanotubes are expected to perform better in repairing, maintaining, restoring, and improving the function of organs and tissues because their inner space can be filled with chemicals, drugs, and biomolecules.[13-15] To date, many methods have been used to prepare TiO_2 nanotubes such as atomic layer deposition,[16] template synthesis,[7, 17-19] anodization,[9, 11, 20] and hydrothermal treatment.[6, 21, 22] Among the various techniques employed so far, the template-assisted sol-gel method has been widely employed to synthesize many metal oxide materials due to its distinct advantages, such as low cost and operating temperature, high chemical homogeneity and purity, and possibility to control material morphology at the nanoscale.[18, 23] So far, various templates have been used for the preparation of TiO_2 nanotubes, including carbon nanofiber,[24] ZnO nanorod,[23] and bacterial flagella.[25] Obviously, the

morphology and structure of the TiO_2 nanotubes are dependent on the templates employed. It has been well accepted that a scaffold should have three-dimensional (3D) porous network structure in order to mimic the structure of natural extracellular matrix (ECM). However, despite significant achievements in the fabrication and characterization of 3D arrays of anodized TiO_2 nanotubes as potential biomaterials,[9, 11, 20, 26] until now, there has been no report in the literature about the fabrication of 3D network-structured mesoporous TiO_2 nanotubes and the evaluation of the potential applications as bone tissue engineering scaffolds.

Herein, we report for the first time the scalable synthesis of a novel 3D porous network-structured scaffold built of mesoporous TiO_2 nanotubes with an extraordinary large surface area and a diameter of less than 100 nm using template-assisted sol-gel approach followed by calcination. We chose bacterial cellulose (BC), a natural polysaccharide synthesized by nonpathogenic microbial strains such as *Acetobacter xylinum* as the template for the synthesis of TiO_2 nanotubes. The rationale of using BC was based upon the fact that BC has intrinsic 3D porous network structure. Furthermore, it has high strength, nano-sized fiber diameter, commercially available and much cheaper than other organic templates.

The aim of this study was to synthesize a TiO_2 nanotube scaffold with 3D network structure, to characterize its morphology and structure, and preliminarily evaluate the biological behavior of this novel scaffold. The loading of biological factors into the nanotube spaces and the release profiles will be investigated in our future studies.

2 Materials and methods

2.1 Preparation of BC aerogels

The preparation procedure of BC pellicles was described in our previous work.[27] Briefly, the bacterial strain, Acetobacter xylinum X-2, was grown in the culture media containing 0.3 wt% analytic grade green tea powder and 5 wt% analytic sucrose for 7 days. The pH of the medium was adjusted to 4.5 by acetic acid. BC pellicles were purified by soaking in deionized water at 90 °C for 2 h followed by boiling in a 0.5 M NaOH solution for 15 min. The pellicles were then washed with deionized water several times and soaked in 1 wt% NaOH for 2 days. After rinsing with deionized water until neutrality, the BC pellicles were finally freeze-dried to obtain BC aerogels.

2.2 Preparation of TiO_2/BC hybrids

Two different solvents (isopropanol and ethanol) were used to prepare TiO_2/BC hybrids. In the case of absolute ethanol, a BC aerogel (approximately 25 mg) was immersed in the mixtures of ethanol/titanium tetra-n-butyl ($Ti(OBu)_4$) with three different concentrations of $Ti(OBu)_4$ (0.1, 0.5, and 1.0 M) for 24 h at room temperature under closed conditions. Afterwards, the product was taken out and rapidly rinsed with ethanol twice and then immersed in a closed vessel containing ethanol and deionized water (volume ratio 9 mL : 1 mL) for 48 h at room temperature to complete the hydrolysis reaction and yield TiO_2/BC hybrids. In the case of isopropanol, the procedures were the same except that ethanol was replaced with isopropanol.

2.3 Preparation of TiO_2 nanotubes

The TiO_2/BC hybrid aerogel was washed with deionized water and freeze-dried in vacuum for 24 h. Finally, calcination was performed in an open tube furnace at 600 °C for 6 h with a heating rate of 1 °C/min to combust the template and to allow crystallization of TiO_2 nanotubes.

2.4 Characterization

Pristine BC, TiO_2/BC, and TiO_2 nanotubes were characterized by scanning electron microscopy (SEM, Nova Nanosem 430), transmission electron microscopy (TEM, Tecnai G2F-20) at an acceleration voltage of 200 kV, and X-ray diffraction (XRD, Rigaku D/Max 2500 v/pc) with Cu K_α radiation. Thermogravimetric analysis (TGA) was performed on a simultaneous TGA/DSC apparatus (STA449F3) with a heating rate of 10 °C/min from room temperature to 800 °C in air atmosphere. Brunauer–Emett–Teller (BET) surface area, pore size and volume of TiO_2 nanotube scaffold were evaluated from nitrogen adsorption isotherms at 77 K using a surface area analyzer (NOVA 2200e). Porosity and pore size distribution of TiO_2 nanotube scaffold was also tested using a mercury intrusion porosimeter (PoreMaster 60GT, Quantachrome Instruments). The compressive properties of TiO_2 nanotube and TiO_2/BC aerogels ($6 \times 6 \times 3$ mm^3) were measured using a micro electromagnetic fatigue testing machine (IBTC-300, Tianjin Care Measure & Control Co., Ltd., Tianjin, China). The strain rate was maintained at 0.2 mm min^{-1}. Five specimens were tested from each sample group.

2.5 Cell proliferation

A mouse fibroblast cell line (L929) and a human osteoblast-like cell line (MG-63)

were used for cell image and proliferation studies. Proliferation of the cells cultured on the sterilized TiO_2 nanotube scaffold specimen was determined by CCK-8 assay. The sterilized specimen was pre-soaked in DMEM for at least 12 h. Then, the specimen was placed into 24-well culture plates and seeded with a cell suspension at a cell density of 8×10^3 cells/mL (L929) or 1.2×10^4 cells/mL (MG-63), followed by culturing for 1 and 3 days at 37 °C in a 5% CO_2 incubator. At predetermined time points, the cell-scaffold constructs were transferred to another culture plate, rinsed with PBS three times to remove non-adhering cells. The cells on the samples were incubated with 50 μL CCK-8 solution for 2 h at 37 °C. After removal of the medium, 500 μL of DMSO (dimethyl sulfoxide) was added to each well. The solution (150 μL) from each well was transferred to a new 96-well cell culture plates and the optical density (O.D.) of each well was read using 490 nm wavelength on a microplate reader machine. The TCPS (tissue culture plate) served as the blank control group.

2.6 Cell imaging

For light microscope observation, the pre-soaked specimen was placed to a well followed by cell seeding (2×10^4 cells/mL) on the specimen. The specimen was left undisturbed in an incubator for 3h to allow the attachment of cells. Afterwards, an additional 1 mL of culture medium was added into each well. The cell/specimen construct was then cultured for up to 7 days under the conditions described above. After incubation at 37 °C in a humidified atmosphere containing 5% CO_2 for 3 days, the cell culture was examined microscopically using an inverted microscope (Leica) for cellular response at the edges of samples since these materials are not

transparent.[28, 29] For SEM observation, after 3 days of cell seeding, the TiO_2 nanotube scaffold was retrieved from the culture plate, rinsed by PBS three times and fixed in 4% paraformaldehyde solution at 4 °C for 12 h, followed by dehydration in ethanol/distilled water series, dried in air, sputter coated with gold, and examined by SEM as aforementioned.

2.7 Alkaline phosphatase (ALP) activity assay

To evaluate alkaline phosphatase (ALP) activity, MG-63 cells were seeded on the TiO_2 nanotube scaffold as described above. For comparison, TCPS and the hydroxyapatite-coated BC nanofibrous (HA/BC) scaffold as reported previously[30] were selected to measure their ALP activity. After the cells were seeded on the specimens and cultured for 1, 4, and 7 days, they were washed twice with PBS followed by trypsinization, collection, and three cycles of freezing and thawing. The as-obtained aliquots of supernatants were subjected to ALP activity and protein content measurements. The ALP activity was determined at 405 nm using p-nitrophenyl phosphate (pNPP, Sigma, St. Louis, MO) as the substrate. Total protein content was determined with the bicinchoninic acid (BCA) method in aliquots of the same samples with the PIERCE (Rockford, IL) protein assay kit. ALP levels were normalized to the total protein content at the end of the experiment, as described in our previous work.[30]

2.8 Calcium content assay

During osteogenic differentiation of MG-63, the amount of calcium deposited on different scaffolds and TCPS was measured. MG-63 cells were seeded at a

concentration of 1.2×10^4 cells/mL on scaffolds in a 24-well tissue culture plate. After 7 and 14 days of incubation, 0.5 N HCl was added to the cells/scaffolds. The supernatant was used for the QuantiChromTM Calcium Assay Kit (DICA-500), according to the manufacturer's instructions (BioAssay Systems, Hayward, CA, USA). Optical density was determined using a microplate reader at a wavelength of 612 nm.

2.9 Statistical analysis

All experiments were performed in triplicate unless otherwise stated. Statistical analysis of data was performed using an SPSS system. All data were presented as mean value ± standard deviation (SD). Results with *p*-values of < 0.05 were considered statistically significant.

3 Results

3.1 Morphology, structure, and mechanical property

We first used ethanol as the solvent for the synthesis of TiO_2/BC hybrids. As shown in Fig. S1, spherical precursors were adsorbed on the surfaces of BC nanofibers regardless of the concentration of $Ti(OBu)_4$. This is ascribed to the high hydrolysis and condensation rates of $Ti(OBu)_4$ in ethanol since the rapid condensation rate of the titanium precursor favors the formation of TiO_2 nanospheres.[31] The high hydrolysis and condensation rates are due to the fact that ethanol has stronger polarity and lower viscosity than isopropanol which makes the hydrolysis and the diffusion faster and easier and makes the resultant TiO_2 particles bigger in size.[32] When isopropanol was used as the solvent, we find that, although no bigger spheres can be found (Fig. S2), the concentration has an impact on the morphology of the TiO_2/BC hybrids. At a

lower $Ti(OBu)_4$ concentration of 0.1M, relatively larger particles on BC surface can be observed (Fig. S2a). When the concentration increases to 0.5 M and 1.0 M, the particles on the surfaces of BC nanofibers become smaller (Fig. S2b) and are hardly discernible by SEM (Fig. S2c), but EDS spectrum confirms the presence of Ti element (Fig. S2d). This finding is in agreement with previous report by Hsu and Nacu who found that a low alkoxide concentration led to a large particle size and a wide size distribution [33] but is in contrast to Wang and Ying's observation that decreasing alkoxide concentration yielded smaller particles.[34] We found that large particle sizes would lead to scaffold collapse during calcination. Therefore, the $Ti(OBu)_4$ concentration of 1.0 M was used in the subsequent investigation.

TEM images (Fig. 1a and b) of the TiO_2/BC hybrids synthesized under optimal sol-gel conditions demonstrate that the surfaces of TiO_2/BC fibers are rough and the particles show irregular shape. This irregular shape of TiO_2 before calcination was also observed by Gutierrez and co-workers.[35] The HRTEM image (Fig. 1c) and SAED pattern (Fig. 1d) reveal the amorphous nature of the TiO_2 before calcination, which is consistent with a previous report.[35]

After calcination at 600 °C for 5 h, the as-prepared TiO_2 nanotubes still sustain the 3D interconnected porous network of pristine BC (Fig. 2a). The inset in Fig. 2a demonstrates the three-dimensionality of the TiO_2 nanotube scaffold. A higher magnification image demonstrates that the surfaces of TiO_2 nanotubes are not smooth although the roughness becomes lower as compared to TiO_2/BC hybrids (Fig. 2b). TEM image (Fig. 2c) demonstrates the tubular structure of the TiO_2 nanotubes and the

porous walls. These structural features are further confirmed by HRTEM image (Fig. 2d). The formation of the porous walls is due to the voids between aggregated TiO_2 nanoparticles. These aggregated nanoparticles also result in rugged tube surfaces, as illustrated in Fig. 2e. Fig. 2d also reveals that the TiO_2 nanotubes are made of many TiO_2 nanoparticles with a size of around 7 nm. The average pore size is 2.9 nm as calculated by the interstice model[36] ($d = (\sqrt{2} - 1) \times D$, where D represents the average diameter of the TiO_2 spheres, around 7 nm). In addition, as shown in Fig. 2d, the clear lattice fringes with an interplanar spacing of 0.352 nm are assigned to the (101) plane of the anatase phase of TiO_2. The SAED pattern (Fig. 2f) demonstrates that the TiO_2 nanoparticles have crystalline structure, suggesting that calcination results in the transition from amorphous to crystalline state. XRD results (Fig. S3) further confirm that the TiO_2 nanotubes are anatase-type, consistent with SAED result. The anatase-type structure of TiO_2 nanotubes is superior to rutile counterpart since the former surpassed the latter in cell adhesion and differentiation.[11, 37] TG-DSC results (Fig. S4) indicate good thermal stability of these TiO_2 nanotubes (the detailed analyses are presented in the ESI).

To determine the pore structure and BET surface area, BC aerogel, TiO_2/BC hybrid aerogel, and TiO_2 nanotube scaffold were examined by N_2 adsorption–desorption experiments. Table S1 summarizes the specific surface area, pore volume, and average pore size obtained from the corresponding N_2 adsorption–desorption isotherms of the three materials. Calculated by the Broekhoff–de-Boer (BdB) spherical pore model, the majority of the pore sizes are

narrowly distributed at 3.3 nm, which is comparable to the calculated value (2.9 nm). The BET surface area of BC aerogel and TiO_2/BC hybrid aerogel calculated from N_2 adsorption/desorption isotherms is 149.9 and 82.5 $m^2 g^{-1}$, respectively, while TiO_2 nanotube scaffold exhibits an extremely high BET surface area of 1629 $m^2 g^{-1}$, which is much larger than many previously reported values.[7, 38-43] The extraordinarily large surface area of TiO_2 nanotube scaffold is due to the 3D porous interconnected structure, mesoporous walls, and rugged surface. To further evaluate the pore distribution of TiO_2 nanotube scaffold, mercury intrusion porosimetry was performed since it can accurately measure pores with a relatively larger size. Fig. S5 displays the pore size distribution obtained by mercury intrusion porosimetry. Note that there are macropores ($\geq$ 50 μm according to literature[44]) in the nanotube scaffold. The dominant pores show a diameter of ca. 92 μm and the porosity is about 76%.

We evaluated the mechanical property of the scaffold by compression testing. Fig. 3 shows the typical compression stress–strain curves of TiO_2 nanotube and TiO_2/BC aerogels. In general, the stress–strain curve for an aerogel (foam) in compression is characterized by three distinct regimes: a linear elastic regime, a collapse plateau regime, and a densification regime.[45] These three regimes are observed in the stress-strain curve of TiO_2/BC, but not noted in the curve of TiO_2 nanotube scaffold. The absence of the first linear elastic regime in the stress-strain curve of TiO_2 nanotube indicates that the scaffold is brittle in nature, which is a common weakness of neat ceramic scaffolds. Following previous reports,[46, 47] we determined the compressive stresses at 80% strain, as defined in literature, which are 45.8 ± 5.6 and

3.5 ± 0.21 kPa for TiO_2/BC hybrid and TiO_2 nanotube, respectively. The much lower strength of TiO_2 nanotube than TiO_2/BC hybrid is attributed to the large number of pores and hollow structure of TiO_2 nanotube. This strength value is also lower than some reported values. For instance, the compressive strength of approximately 2.5 MPa was reported for a TiO_2 scaffold at overall porosity of ~85%.[48] This value is comparable to that of silica aerogel.[49] A previous study found that the measured compressive strength of a hydroxyapatite foam decreased from 1.56 to 0.18 MPa as the porosity was increased from 87 to 95%.[50] This implies that the mechanical weakness of TiO_2 nanotube is mainly due to the abundant existence of pores. Therefore, a trade-off between mechanical property and pore volume should be reached in further investigation.

3.2 Cell behaviors

We then tested cell responses to the TiO_2 nanotube scaffold. We observed cell images around the scaffold since this scaffold is not transparent under inverted microscope. Fig. 4a-d shows representative light micrographs of L929 cells on TCPS (Fig. 4a and b) and at the edges of TiO_2 nanotube scaffold (Fig. 3c and d) after 1 and 3 days culture. Fig. 4e-h shows the light micrographs of MG-63 cells. In all cases, there is no significant difference in cell orientation between the cells around the TiO_2 nanotube scaffold and the cells on the TCPS (far from the scaffold) regardless of the culture time and cell type. In other words, no cell circumambulation around the scaffold can be detected. These findings indicate that the TiO_2 nanotubes do not have negative effect on cell proliferation.

Fig. 5 presents the SEM micrographs of the adhered L929 and MG-63 cells on TiO_2 nanotube scaffold after 3 days culture. The L929 cells spread well on the scaffold and are tightly adhered to the scaffold (Fig. 5a and b). These results suggest that the scaffold supports the attachment and spreading of L929 cells. The similar phenomenon can be observed in Fig. 5c and d. Furthermore, the MG-63 cells on TiO_2 nanotube scaffold show a number of filopodia extending at the leading edges (arrows in Fig. 5d). This indicates that the scaffold can greatly promote cell proliferation and differentiation of MG-63 cells.

To confirm the cell adhesion assay and to quantitatively evaluate the proliferation of cells on the surface of the scaffold, the CCK-8 assay was employed. The results (Fig. 6a) demonstrate that there are significant differences in the O.D. values ($p < 0.01$) between the TCPS and TiO_2 nanotube scaffold after 1 and 3 days culture. In the case of MG-63 cells (Fig. 6b), there is no significant difference in O.D. value ($p > 0.05$) between the TCPS and TiO_2 nanotube scaffold at day 1. After 3 days incubation, however, TiO_2 nanotube scaffold exhibits a significantly larger O.D. value ($p < 0.01$) than the control group does. CCK-8 results suggest that the cells on scaffold exhibit more robust growth and proliferation as compared to these cells on TCPS.

ALP is an important early osteogenic differentiation and biochemical marker of osteoblasts. In this work, ALP activity was examined. Fig. 7a shows the ALP activity of cells cultured on TiO_2 nanotube scaffold, HA/BC scaffold, and TCPS. At day 1, low ALP activity is detected, indicating limited differentiation into osteoblast phenotype. Further incubation into day 4 and day 7 results in significantly higher ALP

activity on all samples. Statistical analysis indicates that the MG-63 cells on TiO_2 nanotube scaffold show significantly higher ALP activity than the blank TCPS at each time point ($p < 0.05$). Furthermore, as shown in Fig. 7a, the ALP activity of TiO_2 nanotube is not significantly different from that of HA/BC at day 4 and day 7 ($p > 0.05$).

Unlike ALP activity, mineralization is considered to be the late marker of differentiation toward osteoblasts. As shown in Fig. 7b, higher amount of deposited calcium is noted on TiO_2 nanotube and HA/BC scaffolds compared to TCPS at day 7 and 14. There was no significant difference between the amount of mineralized calcium on TiO_2 nanotube and HA/BC scaffolds ($p > 0.05$) at day 7. However, we found that the mineralization is significantly lower on TiO_2 nanotube compared to HA/BC at day 14 ($p < 0.05$).

4 Discussion

The aim of this study was to investigate the synthesis of TiO_2 nanotube scaffold and preliminarily evaluate its biocompatibility and osteogenesis. To achieve this goal, we fabricated a series of TiO_2 nanotubes with varying $Ti(OBu)_4$ concentrations and solvents. Although the mechanisms of the sol-gel process is not the focus of this study, our studies demonstrate that the solvent type and the concentration of $Ti(OBu)_4$ determine the morphology of the resultant TiO_2 products, which is in agreement with previous studies which concluded that the processing variables such as solvent type, pH, reaction temperature, water/alkoxide ratio had significant effects on the sol-gel process and the resultant size and morphology of TiO_2 nanostructures.[32, 33, 51] Our

results demonstrate that an optimal $Ti(OBu)_4$ concentration with the solvent of isopropanol can lead to formation of mesoporous TiO_2 nanotubes with 3D interconnected structure.

Our preliminarily cell studies on cell viability, attachment, and proliferation of L929 and MG-63 on TiO_2 nanotube scaffold have demonstrated that the TiO_2 nanotube scaffold does not have any adverse effect on cell viability. CCK-8 results demonstrate that the cell viability is higher on TiO_2 nanotube scaffold in comparison to TCPS. A common marker of early bone cell differentiation is ALP activity and a late marker is calcium deposition. In this study, both ALP activity and calcium content of TiO_2 nanotube scaffold were measured and compared with the HA/BC scaffold. The results of ALP assay indicates that MG-63 cells cultured on TiO_2 nanotube scaffold show higher levels of ALP activity than those cultured on TCPS. More importantly, the ALP activity and calcium deposition of TiO_2 nanotube scaffold are comparable to the HA/BC scaffold at day 7. Although the mineralization is lower on TiO_2 nanotube in comparison to HA/BC at day 14, likely due to the fact that HA is the main constituent of human bones and provides better biomimic environment for osteoblast cells, the ALP activity and calcium deposition measurements suggest that TiO_2 nanotube scaffold favors bone formation. These findings imply that TiO_2 nanotube scaffold exhibits excellent biocompatibility and favorable bone formation ability. The excellent cell behaviors of the TiO_2 nanotube scaffold are ascribed to the following aspects including surface nanoscale topography, mesopores, and ultra-large BET surface area in addition to the chemical cues provided by anatase-type TiO_2

material that offers a biocompatible and bioactive surface for cells.[52] Firstly, TEM and SEM observations reveal that the surfaces of TiO_2 nanotubes are rough with nanoscale topography. It was shown that the surface nanotopography was essential for the tissue acceptance and cell survival and can lead to enhanced osteoblast function.[53, 54] Furthermore, as pointed out by Tan et al., large surface area of the nanostructured surface topography can provide available sites for protein adsorption and thus enhance the cell-implant interaction.[10] These mechanisms were proved by a very recent study conducted by Lv et al. who declared that the nanoscale geometry of TiO_2 nanotubes promoted the osteogenic differentiation of hASCs (human adipose-derived stem cells).[55] Secondly, the nanofiber-like morphology with meso- and macropores was believed to facilitate the adsorption of proteins, promote cell adhesion and formation of filopodia.[56] Mercury intrusion measurement confirms that the diameter of dominant pores is about 92 μm created by the nanotube arrangement, which is close to the recommended pore size (~ 100 μm) for a scaffold used for bone regeneration.[44] The mesopores revealed by N_2 adsorption–desorption experiments can serve as localized reservoirs of nutrients and growth factors and enhance the tissue oxygenation,[57-59] which are essential biological elements for cell growth. The mesopores in the walls are also believed to enhance the mass transportation between nanotubular matrix and the environment.[60] Thirdly, the extraordinarily large surface area of the TiO_2 nanotube scaffold contributes to the enhanced cell behavior since a large surface area facilitates the spreading and proliferations of cells.[61] Lastly, the surface textures which resemble the in vivo ECM was believed to promote cell

spreading.[62] Therefore, alike to nanofibrous scaffolds, the 3D TiO_2 nanotube scaffold that provides an architecture better biomimicking in vivo ECM as compared to TCPS can significantly improve cell functions.[63] Accordingly, the excellent biocompatibility and osteogenic differentiation of TiO_2 nanotube scaffold is mainly a consequence of the synergistic effects of rough surface topology, porous structure, large surface area, and biomimetic 3D architecture. However, how these structural features affect the biological behaviors of TiO_2 nanotube scaffold and the percentage of each contribution are still unclear and will be the focus of our future investigation. The results presented here imply that a scaffold built of tubular TiO_2 is an attractive architecture for bone tissue engineering and regenerative medicine.

5 Conclusions

A novel 3D bone tissue engineering scaffold built of mesoporous TiO_2 nanotubes has been prepared by the template-assisted sol-gel route followed by calcination. In the sol-gel process, BC was used as the template and isopropanol acted as the solvent. The TiO_2 nanotubes synthesized at optimal processing conditions exhibit mesoporous walls which are composed of aggregated TiO_2 nanoparticles with a size of around 7 nm. The stacked TiO_2 nanoparticles make the wall surface rugged with distinct nanotopography. The scaffold built of mesoporous TiO_2 nanotubes sustains 3D porous network structure of pristine BC and exhibits ultra-large BET surface area of 1629 $m^2 g^{-1}$. Cell studies demonstrate that the TiO_2 nanotube scaffold supports attachment, spreading, and proliferation of cells and exhibits improved cell proliferation and enhanced ALP activity and calcium deposition over TCPS control due to the

synergistic effects of surface nanotopography, porous structure, large surface area, and biomimetic 3D architecture besides the nature of TiO_2 material. The TiO_2 nanotube scaffold is expected to be attractive as a scaffold for bone tissue engineering and regeneration.

References

1. A. Fujishima and K. Honda, *Nature*, 1972, **238**, 37-38.
2. S. P. Albu, A. Ghicov, J. M. Macak, R. Hahn and P. Schmuki, *Nano Lett.*, 2007, **7**, 1286-1289.
3. M. Kemell, V. Pore, J. Tupala, M. Ritala and M. Leskelä, *Chem. Mater.*, 2007, **19**, 1816-1820.
4. S. Liu and A. Chen, *Langmuir*, 2005, **21**, 8409-8413.
5. A. Kumar, A. R. Madaria and C. Zhou, *J. Phys. Chem. C*, 2010, **114**, 7787-7792.
6. J. Akilavasan, K. Wijeratne, H. Moutinho, M. Al-Jassim, A. Alamoud, R. Rajapakse and J. Bandara, *J. Mater. Chem. A*, 2013, **1**, 5377-5385.
7. K. Wang, M. Wei, M. A. Morris, H. Zhou and J. D. Holmes, *Adv. Mater.*, 2007, **19**, 3016-3020.
8. K. S. Brammer, S. Oh, J. O. Gallagher and S. Jin, *Nano Lett.*, 2008, **8**, 786-793.
9. K. S. Brammer, S. Oh, C. J. Cobb, L. M. Bjursten, H. v. d. Heyde and S. Jin, *Acta Biomater.*, 2009, **5**, 3215-3223.
10. R. Liu, S. Liang, X.-Z. Tang, D. Yan, X. Li and Z.-Z. Yu, *J Mater Chem*, 2012,

22, 14160-14167.

11. S. Oh, K. S. Brammer, Y. J. Li, D. Teng, A. J. Engler, S. Chien and S. Jin, *Proc. Natl. Acad. Sci.*, 2009, **106**, 2130-2135.

12. C. Guo, J. Xu, Y. He, Y. Zhang and Y. Wang, *Appl. Surf. Sci.*, 2011, **257**, 3798-3803.

13. C. von Wilmowsky, S. Bauer, R. Lutz, M. Meisel, F. W. Neukam, T. Toyoshima, P. Schmuki, E. Nkenke and K. A. Schlegel, *J. Biomed. Mater. Res. B*, 2009, **89**, 165-171.

14. S. Beke, R. Barenghi, B. Farkas, I. Romano, L. Kőrösi, S. Scaglione and F. Brandi, *Mater. Sci. Engin. C*, 2014, **44**, 38-43.

15. S. B. Lee, D. T. Mitchell, L. Trofin, T. K. Nevanen, H. Söderlund and C. R. Martin, *Science*, 2002, **296**, 2198-2200.

16. S. K. Panda, Y. Yoon, H. S. Jung, W.-S. Yoon and H. Shin, *J. Power Sources*, 2012, **204**, 162-167.

17. P. Hoyer, *Langmuir*, 1996, **12**, 1411-1413.

18. J. H. Jung, H. Kobayashi, K. J. van Bommel, S. Shinkai and T. Shimizu, *Chem. Mater.*, 2002, **14**, 1445-1447.

19. M. S. Sander, M. J. Côté, W. Gu, B. M. Kile and C. P. Tripp, *Adv. Mater.*, 2004, **16**, 2052-2057.

20. K. Vasilev, Z. Poh, K. Kant, J. Chan, A. Michelmore and D. Losic, *Biomaterials*, 2010, **31**, 532-540.

21. Q. Chen, W. Zhou, G. H. Du and L. M. Peng, *Adv. Mater.*, 2002, **14**,

1208-1211.

22. C.-C. Tsai and H. Teng, *Chem. Mater.*, 2004, **16**, 4352-4358.

23. K. R. Moonoosawmy, M. Es-Souni, R. Minch, M. Dietze and M. Es-Souni, *CrystEngComm*, 2012, **14**, 474-479.

24. Z. Xing, A. M. Asiri, A. Y. Obaid, X. Sun and X. Ge, *RSC Adv.*, 2014, **4**, 9061-9063.

25. D. Li, B. Mathew and C. Mao, *Small*, 2012, **8**, 3691-3697.

26. K. Das, S. Bose and A. Bandyopadhyay, *J. Biomed. Mater. Res. A*, 2009, **90**, 225-237.

27. Y. Z. Wan, Y. Huang, C. D. Yuan, S. Raman, Y. Zhu, H. J. Jiang, F. He and C. Gao, *Mater. Sci. Engin. C*, 2007, **27**, 855-864.

28. G. Sailaja, P. Ramesh, T. Kumary and H. Varma, *Acta Biomater.*, 2006, **2**, 651-657.

29. H. Wang, Y. Li, Y. Zuo, J. Li, S. Ma and L. Cheng, *Biomaterials*, 2007, **28**, 3338-3348.

30. B. Fang, Y.-Z. Wan, T.-T. Tang, C. Gao and K.-R. Dai, *Tissue Engin. Part A*, 2009, **15**, 1091-1098.

31. K. He, G. Zhao and G. Han, *CrystEngComm*, 2014, **16**, 7881-7884.

32. A. Mahyar and A. Amani-Ghadim, *Micro Nano Lett.*, 2011, **6**, 244-248.

33. J.-P. Hsu and A. Nacu, *Langmuir*, 2003, **19**, 4448-4454.

34. C.-C. Wang and J. Y. Ying, *Chem. Mater.*, 1999, **11**, 3113-3120.

35. J. Gutierrez, A. Tercjak, I. Algar, A. Retegi and I. Mondragon, *J. Colloid*

Interface Sci., 2012, **377**, 88-93.

36. D. Sun, J. Yang and X. Wang, *Nanoscale*, 2010, **2**, 287-292.
37. J. He, W. Zhou, X. Zhou, X. Zhong, X. Zhang, P. Wan, B. Zhu and W. Chen, *J.Mater. Sci. Mater. Med.*, 2008, **19**, 3465-3472.
38. S. Cabrera, J. El Haskouri, A. Beltrán-Porter, D. Beltrán-Porter, M. D. Marcos and P. Amorós, *Solid State Sci.*, 2000, **2**, 513-518.
39. Z. Ding, G. Lu and P. Greenfield, *J. Phys. Chem. B*, 2000, **104**, 4815-4820.
40. T. Kasuga, M. Hiramatsu, A. Hoson, T. Sekino and K. Niihara, *Langmuir*, 1998, **14**, 3160-3163.
41. A. R. Liu, S. M. Wang, Y. R. Zhao and Z. Zheng, *Mater. Phys. Chem.*, 2006, **99**, 131-134.
42. H. Yoshitake, T. Sugihara and T. Tatsumi, *Chem. Mater.*, 2002, **14**, 1023-1029.
43. H. Yu, J. Yu, B. Cheng and J. Lin, *J. Hazard. Mater.*, 2007, **147**, 581-587.
44. V. Karageorgiou and D. Kaplan, *Biomaterials*, 2005, **26**, 5474-5491.
45. B. A. Harley, J. H. Leung, E. C. C. M. Silva and L. J. Gibson, *Acta Biomater*, 2007, **3**, 463-474.
46. M. Liu, C. Wu, Y. Jiao, S. Xiong and C. Zhou, *J Mater Chem B*, 2013, **1**, 2078.
47. M. Liu, L. Dai, H. Shi, S. Xiong and C. Zhou, *Materials Science and Engineering: C*, 2015.
48. H. Tiainen, S. P. Lyngstadaas, J. E. Ellingsen and H. J. Haugen, *J. Mater. Sci. Mater. Med.*, 2010, **21**, 2783-2792.
49. A. H. Alaoui, T. Woignier, G. W. Scherer and J. Phalippou, *J. Non-Cryst.*

Solids, 2008, **354**, 4556-4561.

50. I.-K. Jun, Y.-H. Koh, S.-H. Lee and H.-E. Kim, *J. Mater. Sci. Mater. Med.*, 2007, **18**, 1071-1077.

51. C. Han, J. Andersen, V. Likodimos, P. Falaras, J. Linkugel and D. D. Dionysiou, *Catal. Today*, 2014, **224**, 132-139.

52. S. Zhang, J. Sun, Y. Xu, S. Qian, B. Wang, F. Liu and X. Liu, *Biointerphases*, 2012, **7**, 60.

53. H. Craighead, C. James and A. Turner, *Curr Opin Solid State Mater Sci*, 2001, **5**, 177-184.

54. T. J. Webster, C. Ergun, R. H. Doremus, R. W. Siegel and R. Bizios, *Biomaterials*, 2000, **21**, 1803-1810.

55. L. Lv, Y. Liu, P. Zhang, X. Zhang, J. Liu, T. Chen, P. Su, H. Li and Y. Zhou, *Biomaterials*, 2014.

56. R. Ravichandran, S. Gandhi, D. Sundaramurthi, S. Sethuraman and U. M. Krishnan, *J. Biomater. Sci., Polym. Ed.*, 2013, **24**, 1988-2005.

57. S. Oh, C. Daraio, L. H. Chen, T. R. Pisanic, R. R. Finones and S. Jin, *J. Biomed. Mater. Res. A*, 2006, **78**, 97-103.

58. R. Ravichandran, D. Sundaramurthi, S. Gandhi, S. Sethuraman and U. M. Krishnan, *Microporous Mesoporous Mater.*, 2014, **187**, 53-62.

59. I. Izquierdo-Barba, L. Ruiz-González, J. C. Doadrio, J. M. González-Calbet and M. Vallet-Regí, *Solid State Sci.*, 2005, **7**, 983-989.

60. V. Liu Tsang and S. N. Bhatia, *Adv. Drug Deliver. Rev.*, 2004, **56**, 1635-1647.

61. H. Zhou, X. Wu, J. Wei, X. Lu, S. Zhang, J. Shi and C. Liu, *J. Mater. Sci. Mater. Med.*, 2011, **22**, 731-739.

62. S. L. Goodman, P. A. Sims and R. M. Albrecht, *Biomaterials*, 1996, **17**, 2087-2095.

63. R. Flemming, C. Murphy, G. Abrams, S. Goodman and P. Nealey, *Biomaterials*, 1999, **20**, 573-588.

Figure captions

Fig. 1 Low (a) and high (b) magnification TEM images, HRTEM (c) and EDS spectrum (d) of TiO_2/BC hybrids synthesized under optimal sol-gel conditions.

Fig. 2 Low (a) and high magnification (b) SEM images, TEM photo (c), HRTEM image (d), schematic illustration showing the rugged outer surface (e), and SAED pattern (f) of TiO_2 nanotubes calcined at 600 °C for 5 h (inset in Fig. 2a showing a representative photo of a TiO_2 nanotube scaffold).

Fig. 3 Compressive stress-strain curves of TiO_2 nanotube scaffold and TiO_2/BC hybrid.

Fig. 4 Light micrographs of L929 (a-d) and MG-63 (e-h) on TCPS (a, b, e, f) and TiO_2 nanotube scaffold (c, d, g, h) after 1 (a, c, e, g) and 3 (b, d, f, h) days culture.

Fig. 5 SEM images of L929 (a and b) and MG-63 (c and d) cells grown on TiO_2 nanotube scaffold after in vitro culture for 3 days.

Fig. 6 CCK-8 results of TiO_2 nanotube scaffold using (a) L929 and (b) MG-63 cells, *asterisk* shows significant difference at $p < 0.05$, statistical comparisons were made with respect to TCPS.

Fig. 7 ALP activity (a) and calcium content (b) of MG-63 on TiO_2 nanotube scaffold, HA/BC scaffold, and TCPS during osteogenic differentiation, *asterisk* shows significant difference at $p < 0.05$, statistical comparisons were made with respect to TCPS.

Fig. 1.

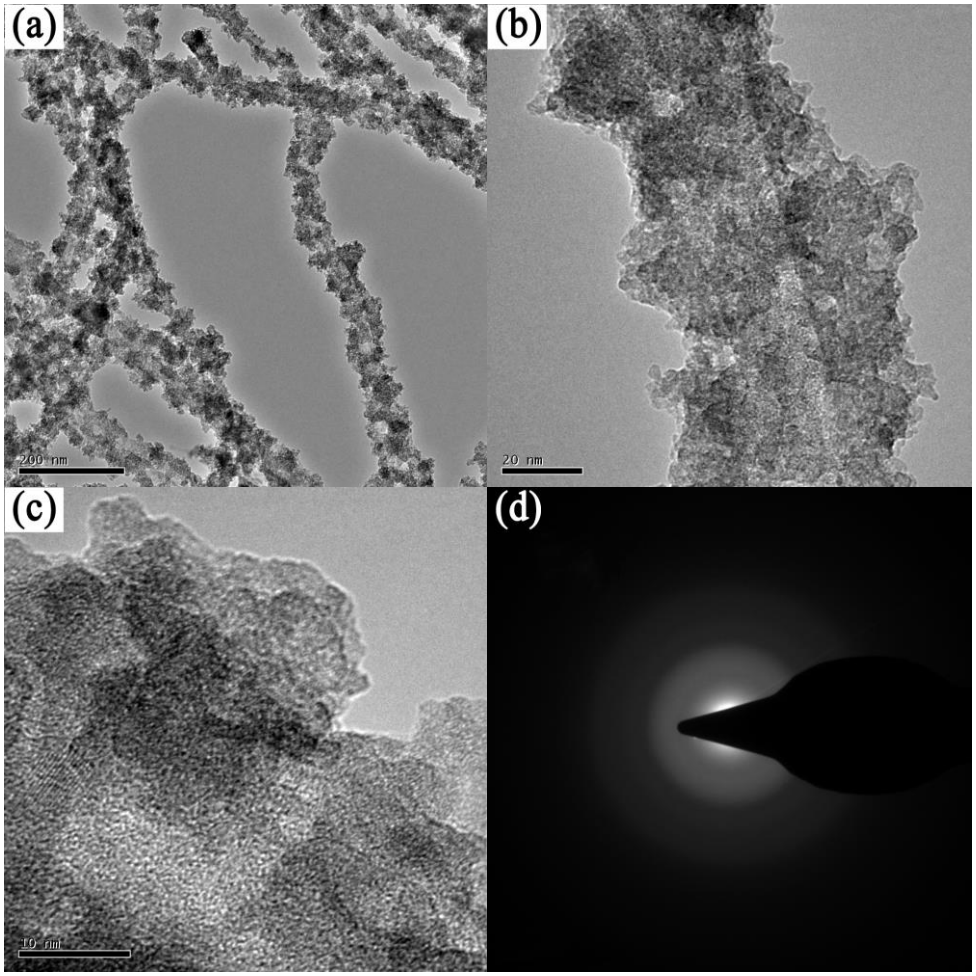

Fig. 2.

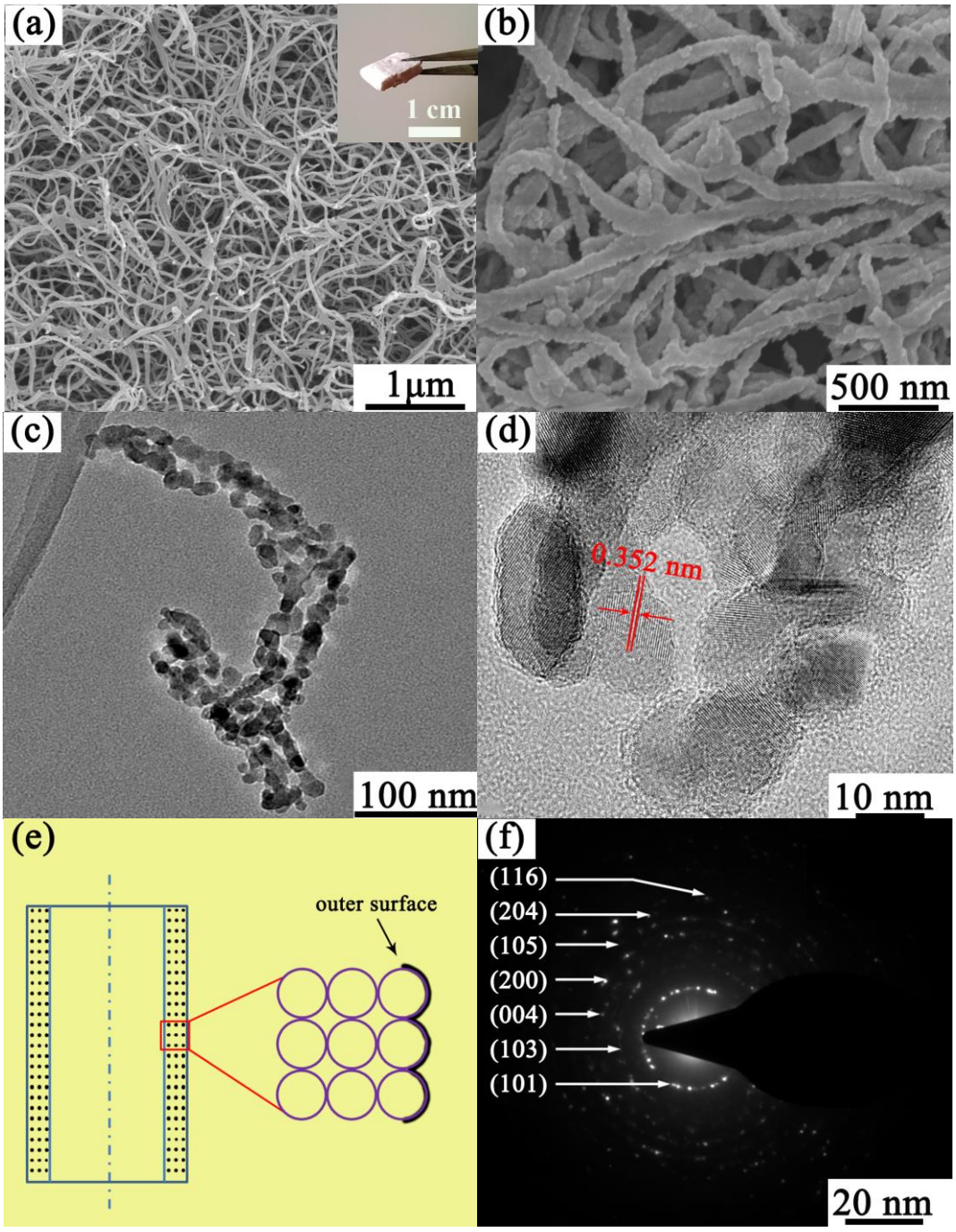

Fig. 3.

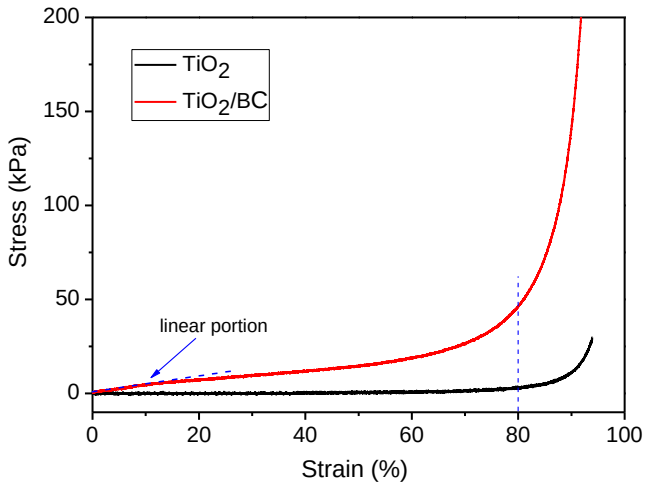

Fig. 4.

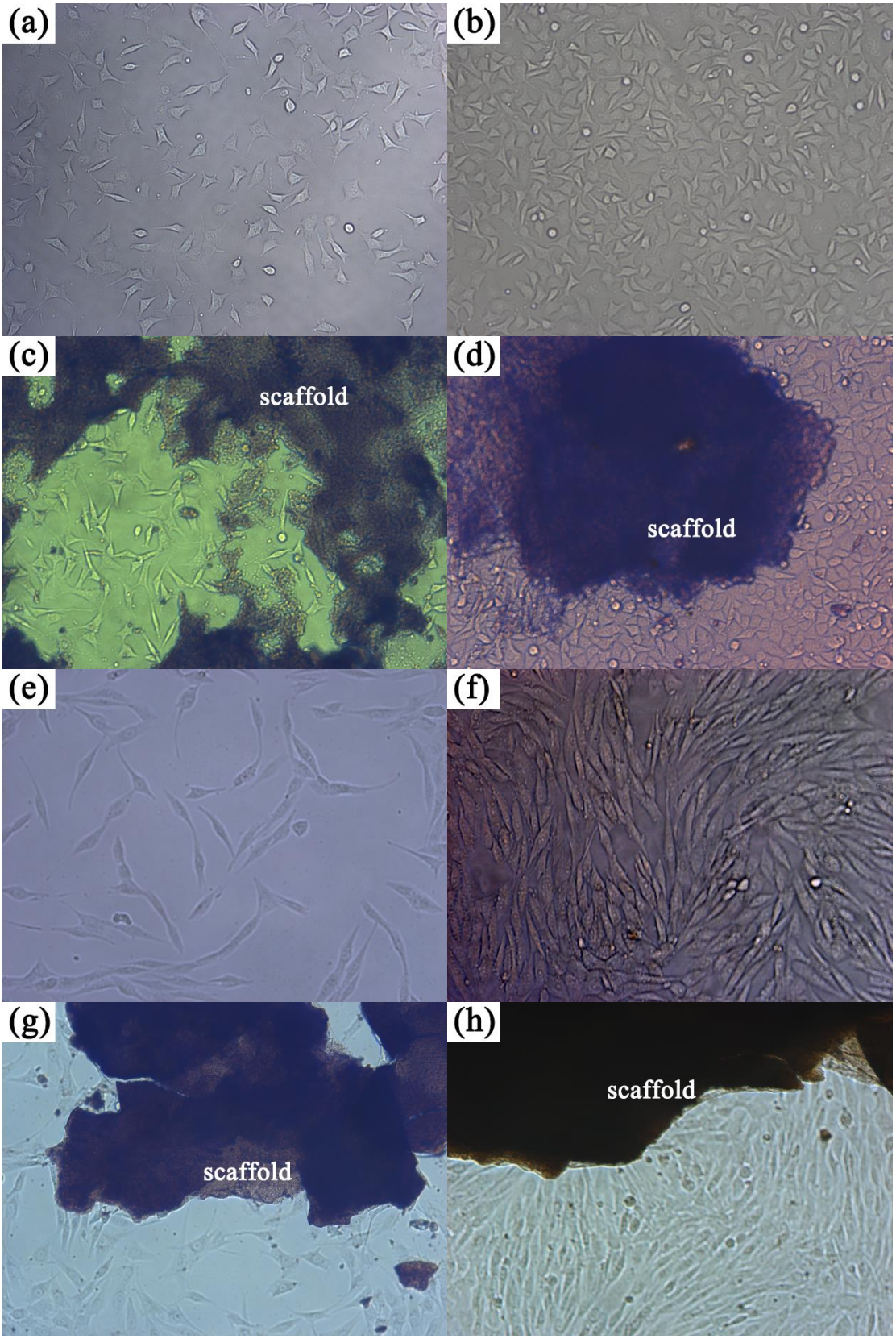

Fig. 5.

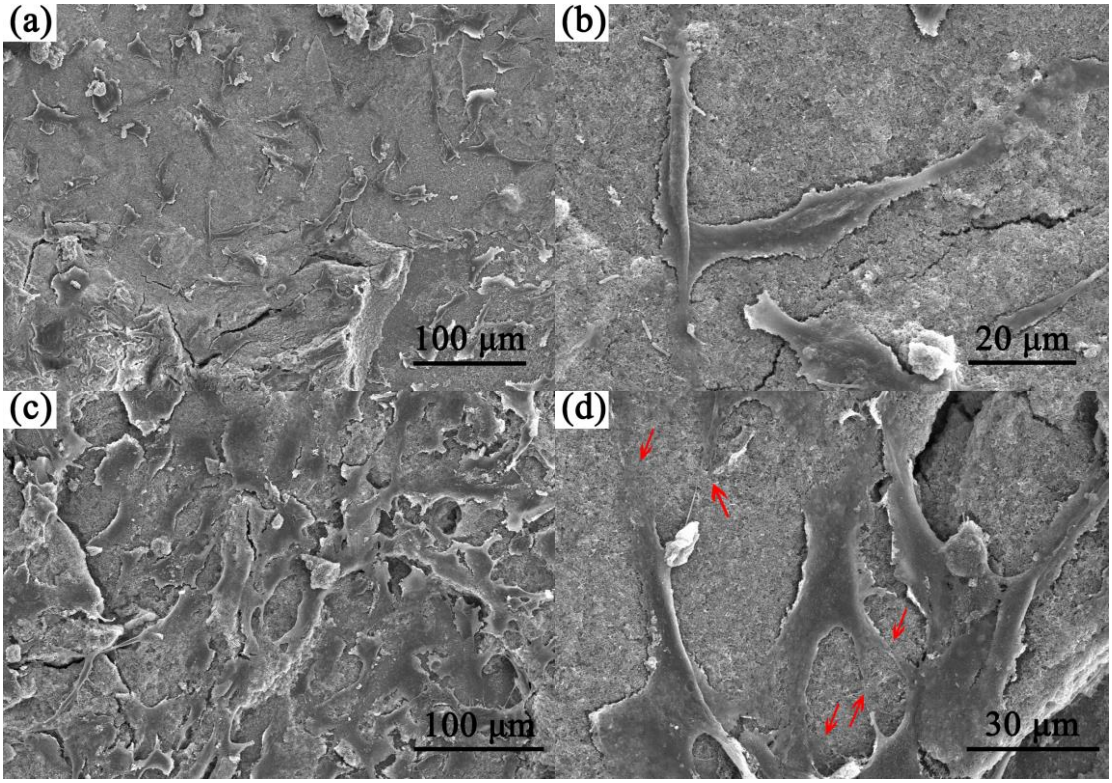

Fig. 6.

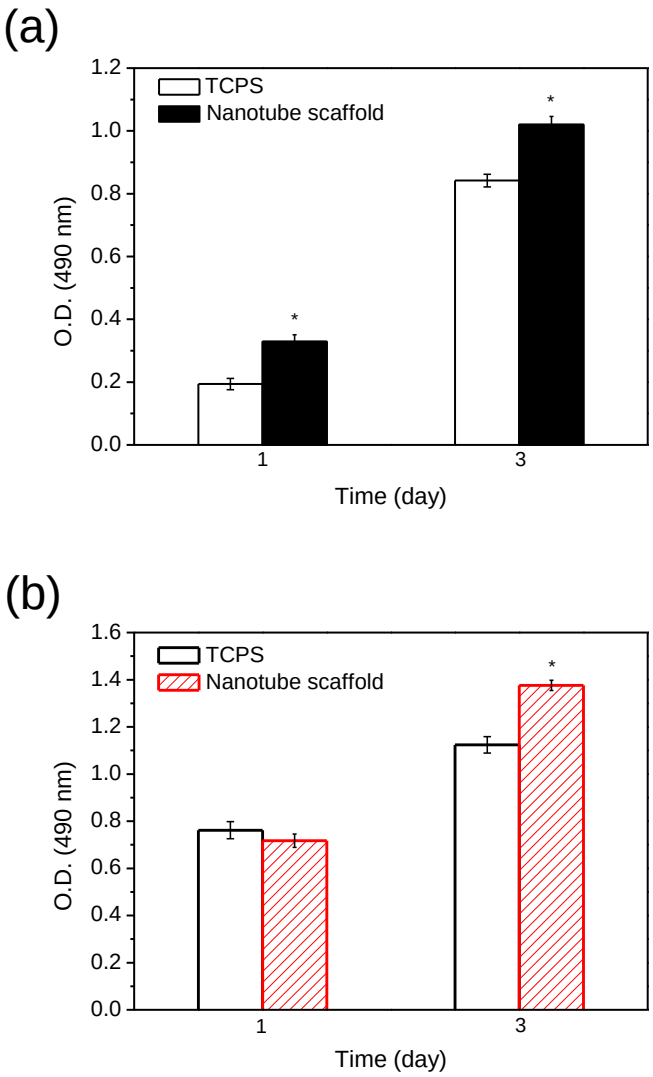

Fig. 7.